biomimetics

MDPI

Article

A Numerical Study of Flow Past a Wall-Mounted Dolphin Dorsal Fin at Low Reynolds Numbers

Zhonglu Lin [1,2,†], Ankang Gao [3,†] and Yu Zhang [1,2,*]

[1] Key Laboratory of Underwater Acoustic Communication and Marine Information Technology of the Ministry of Education, College of Ocean and Earth Sciences, Xiamen University, Xiamen 361005, China; zl352@xmu.edu.cn
[2] State Key Laboratory of Marine Environmental Science, College of Ocean and Earth Sciences, Xiamen University, Xiamen 361005, China
[3] Department of Modern Mechanics, University of Science and Technology of China, Hefei 230026, China; ankanggao@ustc.edu.cn
* Correspondence: yuzhang@xmu.edu.cn
† These authors contributed equally to this work.

Abstract: Dolphin swimming has been a captivating subject, yet the dorsal fin's hydrodynamics remain underexplored. In this study, we conducted three-dimensional simulations of flow around a wall-mounted dolphin dorsal fin derived from a real dolphin scan. The NEK5000 (spectral element method) was employed with a second-order hex20 mesh to ensure high simulation accuracy and efficiency. A total of 13 cases were simulated, covering angles of attack (AoAs) ranging from 0° to 60° and Reynolds numbers (Re) between 691 and 2000. Our results show that both drag and lift increase significantly with the AoA. Almost no vortex was observed at AoA = 0°, whereas complex vortex structures emerged for AoA ≥ 30°, including half-horseshoe, hairpin, arch, and wake vortices. This study offers insights that can inform the design of next-generation underwater robots, heat exchangers, and submarine sails.

Keywords: hydrodynamics; computational fluid dynamics; numerical simulation; dolphin; swimming; bio-locomotion

check for updates

Citation: Lin, Z.; Gao, A.; Zhang, Y. A Numerical Study of Flow Past a Wall-Mounted Dolphin Dorsal Fin at Low Reynolds Numbers. *Biomimetics* **2024**, *9*, 682. https://doi.org/10.3390/biomimetics9110682

Academic Editors: Antonio Concilio and Stanislav N. Gorb

Received: 13 June 2024
Revised: 10 October 2024
Accepted: 30 October 2024
Published: 7 November 2024

Copyright: © 2024 by the authors. Licensee MDPI, Basel, Switzerland. This article is an open access article distributed under the terms and conditions of the Creative Commons Attribution (CC BY) license (https://creativecommons.org/licenses/by/4.0/).

1. Introduction

Dolphin hydrodynamics has long been a topic of interest for fluid dynamists, robot designers, and biologists [1–9]. The dolphin's dorsal fin plays a crucial role in its underwater propulsion and manoeuvring, contributing to its adaptability to various aquatic environments. Studying the hydrodynamic mechanisms of the dorsal fin can provide insights into both biological understanding of cetaceans [10] and innovative engineering designs for biomimetic underwater robotics [11], heat exchangers [12], and submarine sails [13].

Hydrodynamic studies focusing specifically on the dolphin dorsal fin are relatively rare, and a comprehensive study of the *near-fin flow structure* is yet to be conducted. While previous research has focused on dolphin swimming, with particular emphasis on *dynamic propulsion* [7,14] and leaping behaviour above water [15], the current study is more relevant to gliding movements in dolphin-like swimmers [16–18]. Pavlov and Rashad [19] conducted numerical simulations of flow past a static dolphin body with a dorsal fin, demonstrating the minimal hydrodynamic impact of a device attached to the dolphin. Niño-Torres et al. [10] discovered high similarities in the dorsal fin shapes of common bottlenose dolphins in the Caribbean Sea, closely resembling the fin geometry used in this study. Okamura et al. [20] found that the dorsal fin, along with the pectoral fins, enhances stability during straight-line locomotion in small cetaceans, such as dolphins. Inspired by the streamlined shape of the dolphin dorsal fin, Bashtani et al. [12] designed a double-tube

heat exchanger with reduced friction loss. Han et al. [7] applied the immersed boundary method to study a forward-swimming dolphin with an attached dorsal fin and pectoral fins, analysing the surface pressure distribution. Tanaka et al. [21] measured the time-varying kinematics of a dolphin during burst acceleration, providing a scanned geometry of the dolphin, where the dorsal fin was adapted and applied in the present study. Finally, Rahmani et al. [13] utilised the dolphin dorsal fin shape as the sail of a submarine.

Although the *dynamic* whole-body swimming dolphin has already been studied, e.g., [14], it remains valuable to study the flow past a *static* wall-mounted dolphin dorsal fin. The *static* condition is more relevant for certain applications, such as bionic heat exchangers [12] and submarine sails [13], where the detailed 3-D vortex structure has yet to be fully explored. Moreover, in addition to continuous locomotion, dolphins in nature use gliding as an energy-saving strategy during swimming, making the flow past a *static* wall-mounted dorsal fin particularly relevant. For instance, adult bottlenose dolphins (*Tursiops truncatus*) can glide up to 16 metres during a dive [16]. Similarly, newborn dolphin calves (0–1 month old) of the same species spend about one-third of their time gliding [22] rather than actively propelling themselves. It is hypothesised that during gliding over such distances, the flow structure around the dolphin is markedly different from that of an actively propelling dolphin. Additionally, several studies on dolphin-inspired robots have focused specifically on gliding [17,18]. To the best of our knowledge, the unique vortex structures identified in this study have not been previously documented. Therefore, despite the pioneering research on dolphin swimming, the authors believe that investigating this *static* problem remains valuable.

In summary, no comprehensive study has yet focused on the 3-D flow structures near a dolphin's dorsal fin, despite its potential applications [11–13,23]. Thus, in this paper, we investigate the hydrodynamics of flow past a wall-mounted dorsal fin, with an emphasis on its vortical structures at Reynolds numbers ranging from 691 to 2000, based on the dorsal fin's base chord length, and angles of attack (AoAs) from 0° to 60°. As live dolphins, dolphin robots, or submarine sails resembling a dorsal fin all glide during forward propulsion, they frequently encounter underwater currents from various angles of attack. Dolphins have evolved to be highly adapted to the dynamic underwater environment, so it should be reasonable to postulate that their dorsal fins have evolved to provide advantages in such situations, making them worthy of investigation. Dolphins can glide at an average speed of 1.47 m/s [16], corresponding to $Re = 10^5$ in the present study. However, because of constraints in computational resources, the maximum Re simulated in this study is 2000. Nevertheless, it is not uncommon to use low-Reynolds number (10^3) simulations to discuss moderate-Reynolds number (10^5) experimental results [24].

2. Computational Methods

This section outlines the methodology used in the study. We employ the open-source software NEK5000 [25] to generate accurate spectral element solutions for the flow around a wall-mounted dolphin dorsal fin subjected to steady currents, with varying Reynolds numbers (Re) and angles of attack (AoAs). Additionally, a mesh independence study is conducted to ensure the accuracy of the results. Further validation is provided in Appendix A. In this study, the Reynolds number is defined based on the fin's chord length C as $Re = UC/\nu$, where ν is the kinematic viscosity and U is the free-stream velocity.

2.1. NEK5000

NEK5000 [25], which is based on a spectral element method, is an open-source package developed at Argonne National Laboratory. It is known for its scalability, efficiency, and capacity to handle unstructured mesh, which is essential for the curved surface of a dolphin dorsal fin. In NEK5000, the governing equation of incompressible Navier–Stokes equations [26] with constant fluid properties can written as

$$\frac{\partial \mathbf{u}}{\partial t} = -\mathbf{u} \cdot \nabla \mathbf{u} - \nabla p + \frac{1}{Re} \nabla^2 \mathbf{u} + \mathbf{f}, \quad \nabla \cdot \mathbf{u} = 0, \tag{1}$$

where $\mathbf{u} = \{u, v, w\}^{\mathrm{T}}$ is the velocity vector, p is the pressure, and $\mathbf{f}$ is the body-force term. NEK5000 is particularly advantageous for handling complex vortex structures and flow fields while maintaining high accuracy. It has also been successfully applied to studies involving accelerating swimmers [27]. In the spectral element method (SEM) [28,29], the physical domain is divided into spectral elements. The local approximation of the flow field is then represented as a sum of Lagrange interpolants, which are defined by an orthogonal basis of Legendre polynomials up to degree N. The same polynomial order N is applied in all spatial directions, with a P_N–P_N spatial discretisation employed [25]. In most simulations, $N = 3$ is used. The equations are advanced in time with a second-order conditionally stable backward differentiation and extrapolation scheme (BDF2/EXT2) [30,31], using an implicit approach for the diffusion term and an explicit approach for the advection term. NEK5000 is highly parallelised and scalable, capable of running on thousands of threads [32]. The results presented in this study were obtained using 64 to 128 processors.

2.2. Problem Setup

This section outlines the setup of the representative problem. As shown in Figure 1, within a rectangular computational domain, a dolphin dorsal fin is mounted on the bottom wall and is subjected to a steady current of incompressible fluid. Both the dorsal fin and the bottom wall are treated as no-slip boundaries. The inlet velocity is uniform at U. Symmetry boundary conditions are applied to the side walls and top wall, effectively acting as slip boundaries. The geometry of the dolphin dorsal fin (Figure 2) is adapted from the scan of a frozen dolphin (*Lagenorhynchus obliquidens*) by Tanaka et al. [21]. For boundary conditions, at the inlet, Dirichlet conditions are prescribed as $\{u, v, w\}^{\mathrm{T}} = \{U, 0, 0\}^{\mathrm{T}}$. For non-stress formulation, the outlet boundary condition can be written as $[-p\mathbf{I} + \nu(\nabla \mathbf{u})] \cdot \hat{\mathbf{e}}_n = 0$. The symmetric boundary ("SYM" in Figure 1) is prescribed as $\mathbf{u} \cdot \hat{\mathbf{e}}_n = 0$, $(\nabla \mathbf{u} \cdot \hat{\mathbf{e}}_t) \cdot \hat{\mathbf{e}}_n = 0$, $(\nabla \mathbf{u} \cdot \hat{\mathbf{e}}_b) \cdot \hat{\mathbf{e}}_n = 0$. Here, $\hat{\mathbf{e}}_n$ is the unit normal vector, $\hat{\mathbf{e}}_t$ is the unit tangent vector, and $\hat{\mathbf{e}}_b$ is the unit bitangent vector. The wall boundary condition is $\mathbf{u} = 0$.

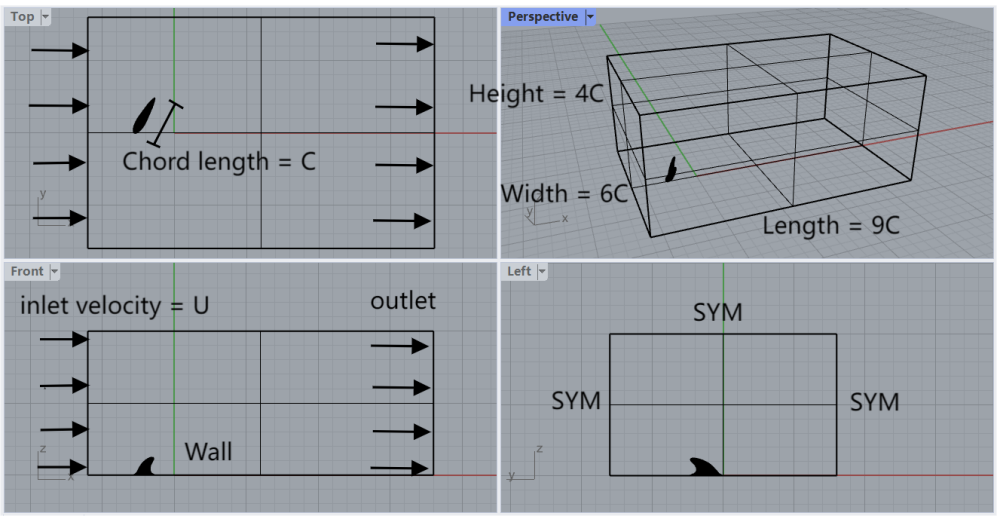

Figure 1. Schematics showing the problem setup, where the "SYM" is the symmetric boundary condition and the "Wall" is the non-slip boundary. "C" is the characteristic length.

A grid independence study was performed to ensure the selection of an appropriate mesh, as shown in Figure 3. The mesh with 71,612 elements was chosen for the current study.

The drag coefficient is defined as $C_d = 2F_x/(\rho U^2 A)$, where F_x is the force in the streamwise direction, ρ is the fluid density, and A is the reference area of the fin at AoA $= 0°$

projected onto the side plane. Global and close-up views of the mesh can be found in Figures 4 and 5, respectively.

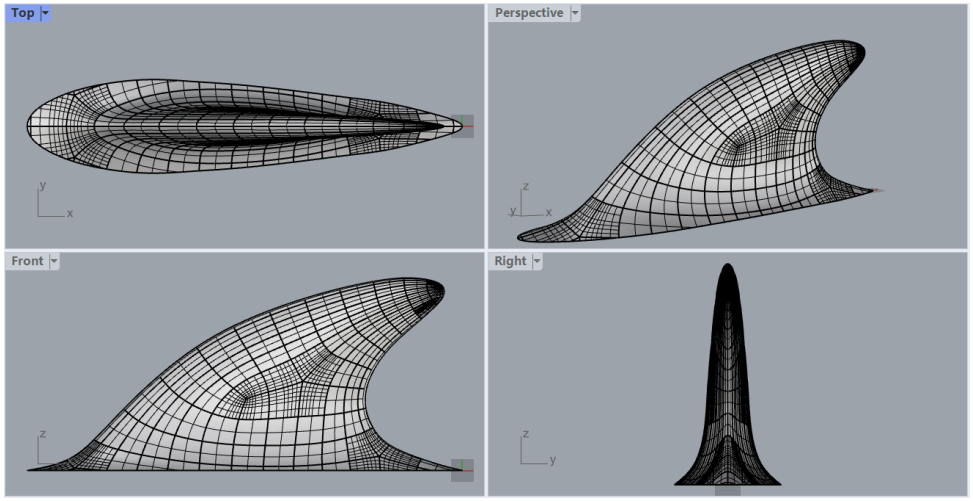

Figure 2. Close-up view of the mesh on the dolphin dorsal fin, adapted from Tanaka et al. [21].

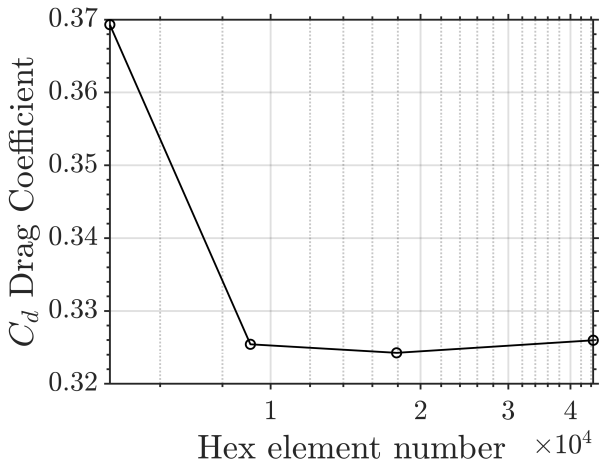

Figure 3. A grid convergence study was conducted at $Re = 691$ and AoA $= 0°$ for four meshes of various mesh densities. The drag coefficient quickly converges at the second mesh. The mesh of 71,612 hex elements was chosen for this paper's simulations. The CFL number was controlled at approximately 0.5 for all the simulations. The number of Gauss–Lobatto–Legendre points per element in each spatial direction was fixed at four.

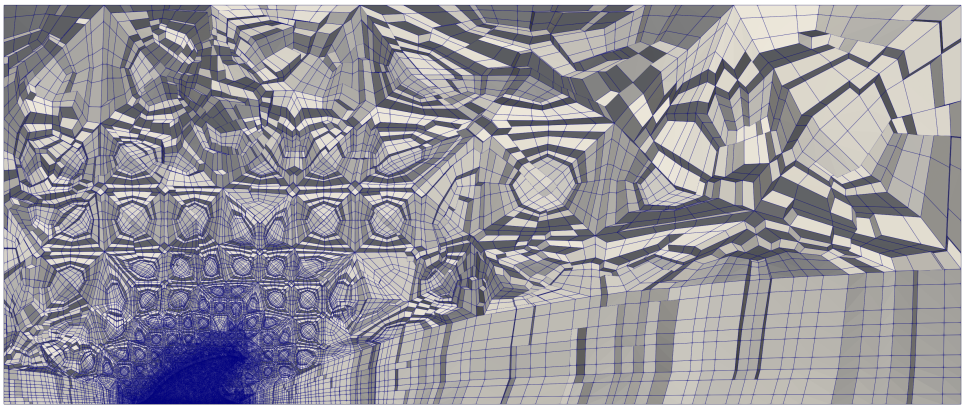

Figure 4. A clipped overview of the selected unstructured pure hex mesh. A non-linear quadratic mesh was applied.

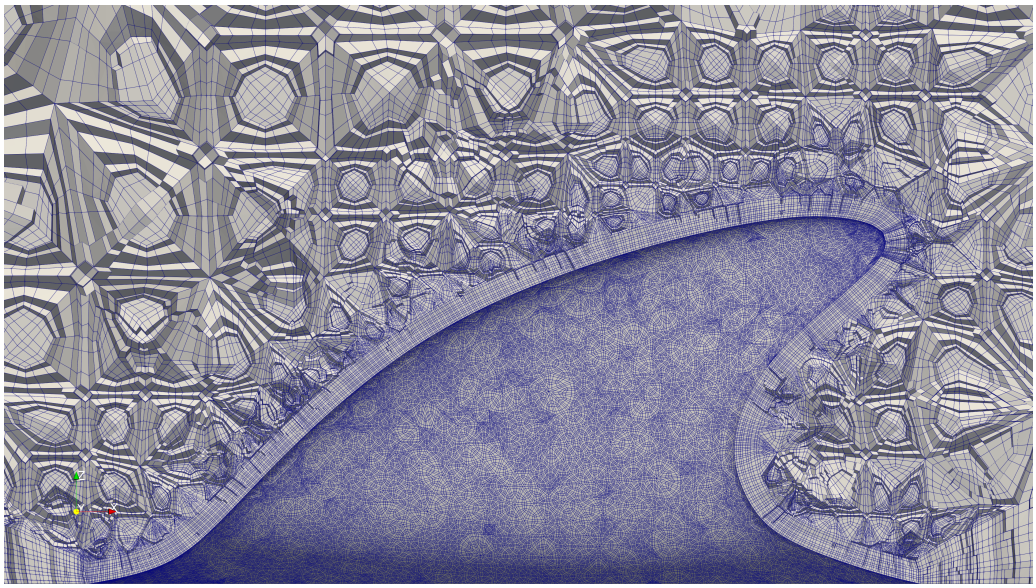

Figure 5. A clipped close-up view of the selected mesh near the dolphin dorsal fin.

3. Discussion of Numerical Results

Simulations were carried out at Re = 691–2000 and AoA = 0°–60°. We analysed the results by examining the drag coefficient and the isosurfaces of the Q-criterion, pressure, and velocity magnitude. The force coefficient and flow structure show minimal variation with Re but significant changes with AoA. Therefore, our discussion focuses primarily on the variation with AoA.

At low Re = 691–2000, the drag and lift coefficients both increase with the AoA. As shown in Figure 6a, increasing the AoA from 0° to 60° results in more than a fivefold increase in drag (C_d). In Figure 6b, the lift coefficient (C_L) rises from 0 at AoA = 0° to approximately 1.5 at AoA = 30° before reaching a plateau between AoA = 30° and 60°. Regarding the effect of the Reynolds number, drag decreases slightly as the Reynolds number increases, while the lift coefficient remains largely unaffected by changes in the Reynolds number.

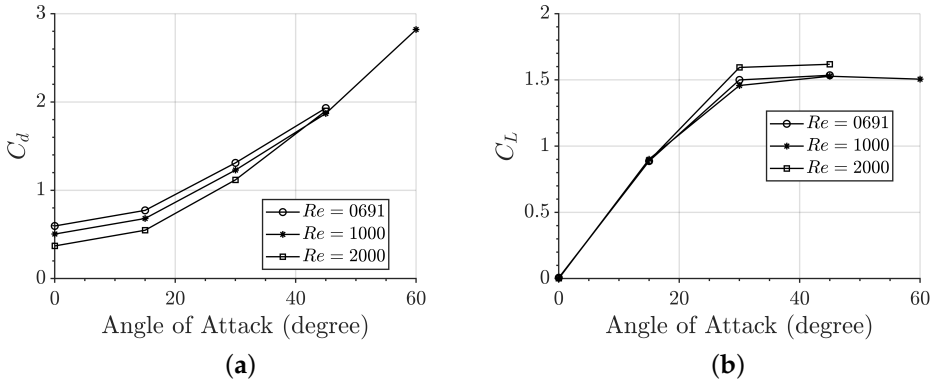

Figure 6. Variations in the (**a**) drag coefficient C_d and the (**b**) lift coefficient C_L at AoA = 0–60° and Re = 691–2000.

Flow Structure by Q-Criterion Isosurface

The Q-criterion is used to visualise the 3-D vortical structures, with a dimensionless value of $Q^* = Qc^2U^2 = 7.7$, as seen in Figures 7–9 and A5. In the following discussion, the naming of vortex types follows conventions established in studies involving flow past wall-mounted objects [33–36]. As depicted in Figures 7 and 9, the flow structure becomes significantly more complicated as AoA increases from 0° to 60°. Generally, the geometry of the dolphin fin avoids the complex flow structures typically seen at AoA $\leq$ 30°; in contrast,

a square cylinder in a similar Reynolds number range produces much more intricate flow patterns [33].

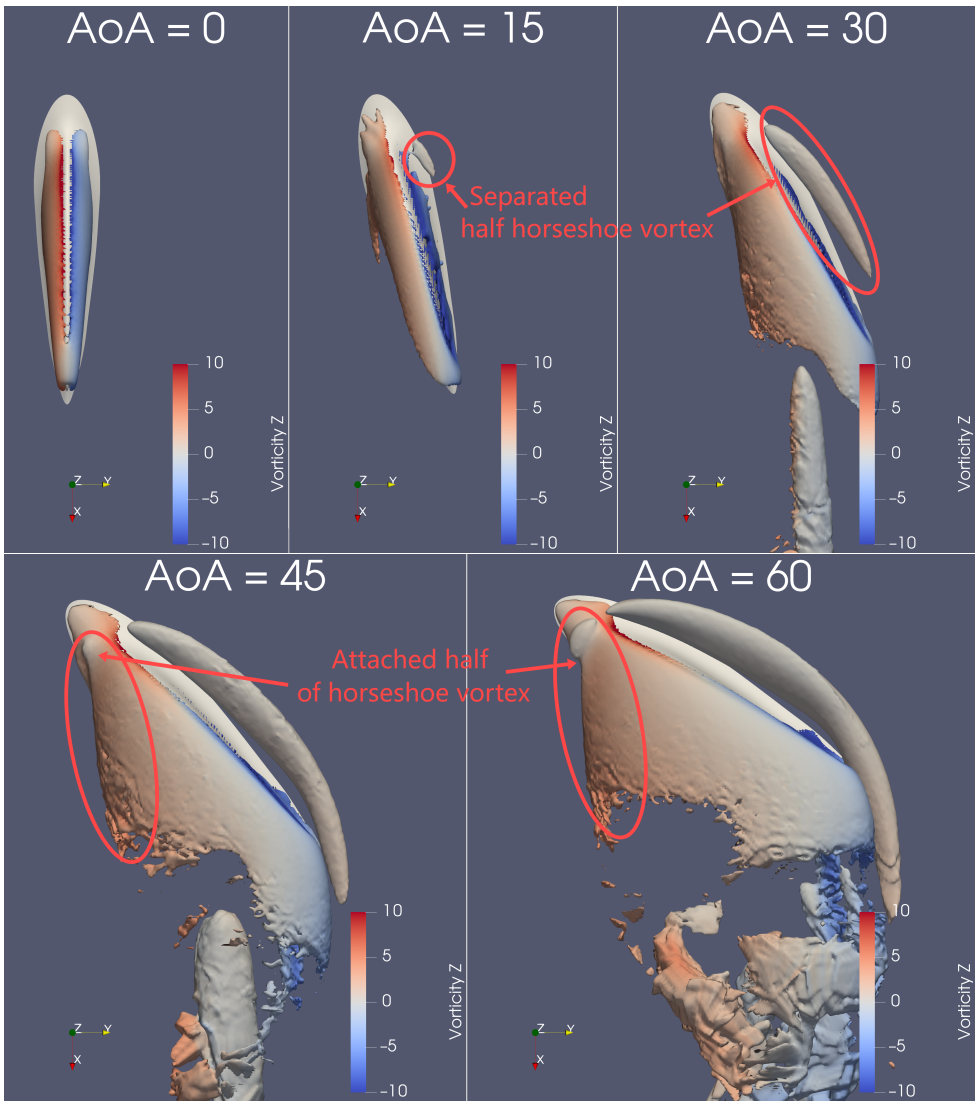

Figure 7. At $Re = 1000$ and AoA = 0–60°, the isosurface of $Q^* = 7.7$ is coloured by vorticity in the Z-direction viewed from the top. The separated half-horseshoe vortex is found near the upstream side, whereas the attached half-horseshoe is upon the downstream surface and near the leading edge.

At AoA = 0°, the flow pattern is symmetric, with no significant flow separation. In this configuration, the dorsal fin is aligned with the incoming flow, and its streamlined geometry effectively minimises the formation of surrounding vortices. This starkly contrasts the flow patterns observed at higher angles of attack (AoA $\geq$ 30°) and the behaviour of bluff bodies at low Reynolds numbers [33,34].

At AoA $\geq$ 30°, abundant flow structures emerge, which correspond to the plateauing of the lift coefficient (C_L) observed in Figure 6b. Two halves of the *horseshoe* vortices form on either side of the dorsal fin at AoA $\geq$ 30°, as shown in Figures 7 and 8. One half detaches from the dorsal fin, resembling the horseshoe vortex structure seen around a square cylinder [33], while the other half remains attached to the fin, merging with the arch vortex, as depicted in Figure 9.

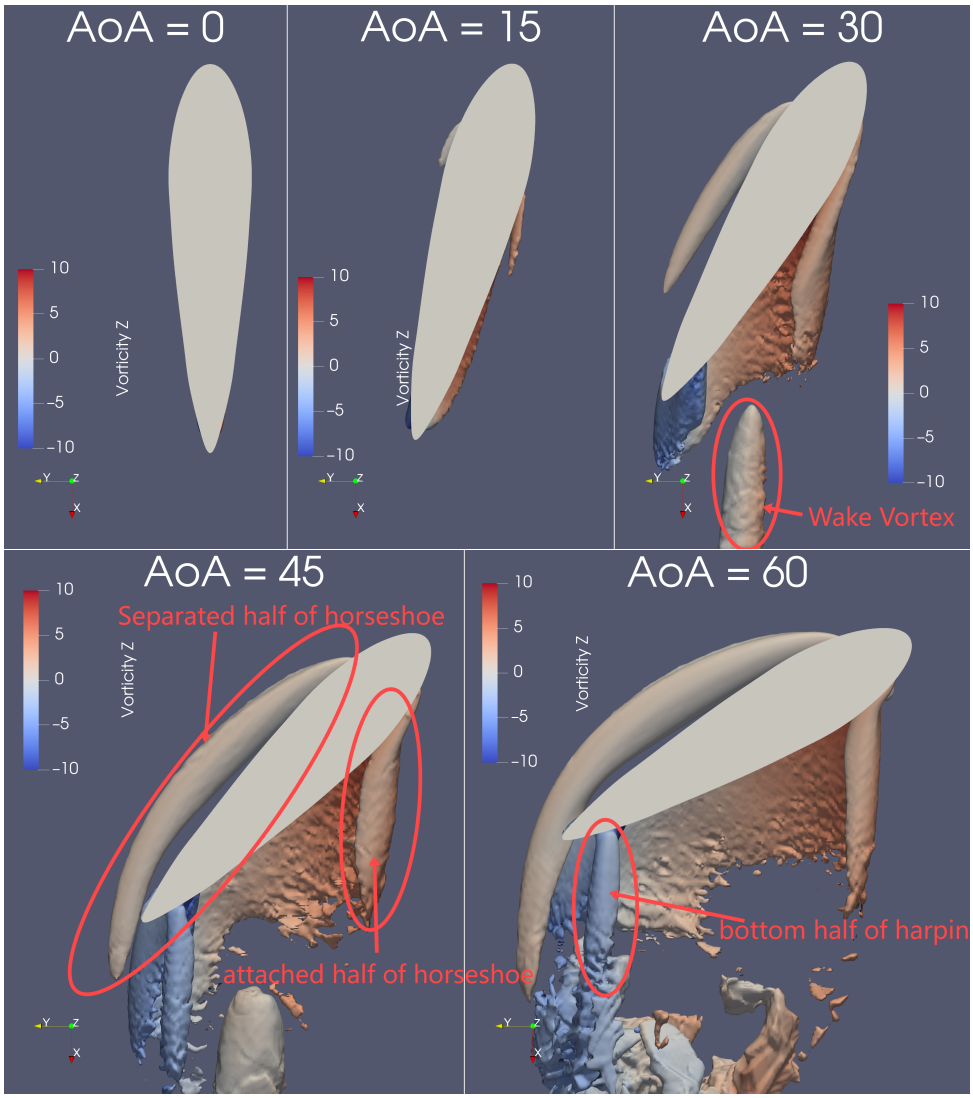

Figure 8. At $Re = 1000$ and AoA $= 0$–$60°$, the isosurface of $Q^* = 7.7$ is coloured by vorticity in the Z-direction, viewed from the bottom. The two halves of the horseshoe vortices can be seen clearly from the bottom angle; both develop significantly with the AoA. The attached half of the horseshoe merges with the arch vortex. The bottom half of the hairpin vortex appears at AoA $\geq$ 30 while extending with AoA.

The separated half of the horseshoe vortex can be observed on the right side of the dorsal fin when viewed from above, as shown in Figure 7. As AoA increases, the separated half-horseshoe extends around the right side of the dorsal fin and into the wake. At AoA $= 15°$, this vortex is barely noticeable, but at AoA $= 30°$, its length increases more than fourfold. From AoA $= 30°$ to $45°$, its size doubles, with its length rising by another 1.5 times. By the time AoA reaches $60°$, the half-horseshoe vortex shows only minor size expansion and slight further lengthening. Thus, the separated half of the horseshoe vortex undergoes significant changes only within the range of AoA = $15°$–$45°$.

Similarly, the attached half-horseshoe vortex can be seen on the left side of the dorsal fin when viewed from above, as illustrated in Figure 7. For a clearer view of the attached vortex, a bottom perspective, as shown in Figure 8, better reveals its extension with increasing AoA. At AoA $= 15°$, the attached vortex is barely visible, but by AoA $= 30°$, both its length and size double. However, from AoA $= 45°$ and beyond, the attached vortex maintains its size and length. Therefore, the attached half of the horseshoe vortex exhibits significant changes only in the range of AoA = $15°$–$30°$, which does not align precisely with the changes observed in the separated vortex.

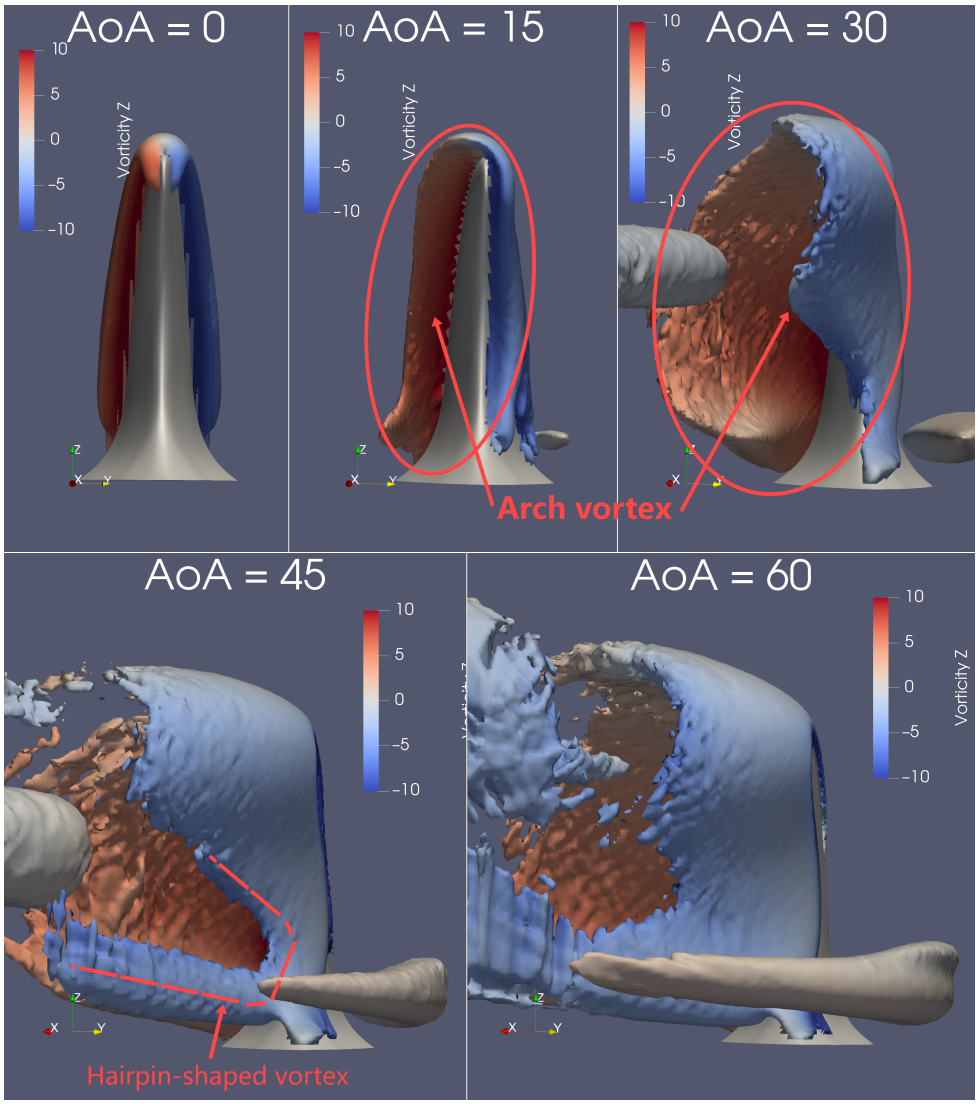

Figure 9. At $Re = 1000$ and AoA = 0–60°, the isosurface of $Q^* = 7.7$ is coloured by vorticity in the Z-direction, viewed from the back and along the fin's symmetric plane at each angle of attack. As AoA increases, the enveloping arch vortex tilts up and extends further from the downstream side of the dorsal fin, eventually merging with the hairpin-shaped vortex at AoA = 60°.

A layer of the arch vortex forms closely above the dorsal fin, as shown in Figure 9. As AoA increases, the arch vortex tilts upwards and extends further downstream from the dorsal fin, eventually merging with the hairpin-shaped vortex. At AoA = 0°–15°, the arch vortex exhibits only a slight tilt, while at AoA = 30°, it extends approximately three times further downstream. At AoA = 45°, the arch vortex on the back of the fin extends about twice as much, connecting with the base vortex to form a hairpin-shaped structure. The shape of this arch vortex is similar to those observed in the flow around a square cylinder [33,36].

The "hairpin-shaped vortex" is particularly noteworthy. In this case, the U-shaped vortex emerges immediately from the crescent-shaped curve on the back of the dolphin dorsal fin, which differs from square-cylinder scenarios where hairpin vortices form further downstream because of a different mechanism. A view of the hairpin vortex from another angle is shown in Figure A5.

The wake vortex is also an interesting aspect to discuss. It forms at AoA = 30°–60°, as seen in Figures 7 and 8, and its size increases with AoA. The single wake vortex at AoA = 30° extends directly downstream, which contrasts sharply with the more complex flow structures observed in the wake of a finite square cylinder at similarly low *Re* [33,35].

In addition, further observations of the flow structure were conducted by reviewing the distribution of pressure and velocity magnitude, as shown in Appendix Pressure and Velocity Distribution.

4. Conclusions

In this study, we presented a numerical investigation of the flow past a wall-mounted dolphin dorsal fin at angles of attack (AoAs) ranging from 0° to 60° and low Reynolds numbers between 691 and 2000. These simulations offer insights into the fundamental flow structures that arise when a dolphin glides through oblique currents or performs turning manoeuvres in water. Both drag and lift increase significantly with AoA, while drag shows only a slight decrease with increasing Reynolds number. The vortex structures, pressure, and velocity magnitude distributions vary substantially with AoA, and these variations generally align with changes in the lift coefficient. At AoA $= 0°$, the streamlined shape of the dorsal fin suppresses almost all vortex formation. At AoA $\geq 30°$, several distinct vortical structures emerge, which are generally simpler than those observed around a square cylinder at similar Reynolds numbers. Notably, two half-horseshoe vortices are observed: one upstream, which separates from the fin, and another downstream, which remains attached to the fin. A hairpin-shaped vortex appears near the trailing edge, while an arch vortex envelops the downstream fin surface, connecting the attached half-horseshoe vortex with the hairpin vortex. A clear single wake vortex is found at AoA $= 30°$ and 45°. The pressure magnitude generally increases with AoA, and the velocity magnitude on the upstream side of the fin also rises as AoA increases.

This study is limited by the assumption of a rigid fin, as it does not account for fluid–structure interactions of the flexible dorsal fin. Future work will incorporate these interactions to understand the dorsal fin's function better. Additionally, we plan to explore higher Reynolds numbers in future studies.

Author Contributions: Conceptualisation, Z.L. and A.G.; methodology, Z.L. and A.G.; software, Z.L. and A.G.; validation, Z.L.; formal analysis, A.G.; investigation, Z.L. and A.G.; resources, Y.Z.; data curation, Z.L.; writing—original draft preparation, Z.L.; writing—review and editing, A.G.; visualisation, Z.L. and A.G.; supervision, A.G. and Y.Z.; project administration, Y.Z.; funding acquisition, A.G. and Y.Z. All authors have read and agreed to the published version of the manuscript.

Funding: We sincerely appreciate the technical assistance regarding NEK5000 from Dr. Xing-Liang Lyu. This work was funded by the Fujian Provincial Department of Human Resources and Social Security 2023–2024 Visiting Scholar and Research Fellowship Program for High-Level Talents and Outstanding Young Talents, China Postdoctoral Science Foundation (Grant No. 2021M691865); the National Natural Science Foundation of China, 12302320; the Science and Technology Major Project of Fujian Province in China (Grant No. 2021NZ033016); the Special Fund for Marine and Fishery Development of Xiamen (Grant No. 20CZB015HJ01); and the Water Conservancy Science and Technology Innovation Project of Guangdong (Grant No. 2020-16). This work was also financially supported by the National Natural Science Foundation of China (Grant Nos. 12074323; 42106181), the Natural Science Foundation of Fujian Province of China (No. 2022J02003), the China National Postdoctoral Program for Innovative Talents (Grant No. BX2021168), and the Outstanding Postdoctoral Scholarship, State Key Laboratory of Marine Environmental Science at Xiamen University.

Data Availability Statement: Data are available upon request.

Conflicts of Interest: The authors declare no conflicts of interest.

Appendix A. Validation

To validate the computational setup used in this study with NEK5000, we selected a benchmark case of flow past a finite-length square cylinder, as shown in Figures A1 and A2. The problem setup mirrors that used in [33,34], with a Reynolds number $Re = 250$ and an aspect ratio $AR = 4$, calculated by dividing the characteristic length by the cylinder height.

The model was validated against the results from [33,34], as presented in Table A1. The converged mean drag coefficient (C_d) from our model, 1.230, closely matched the values reported by Zhang et al. (1.213) and Saha (1.23).

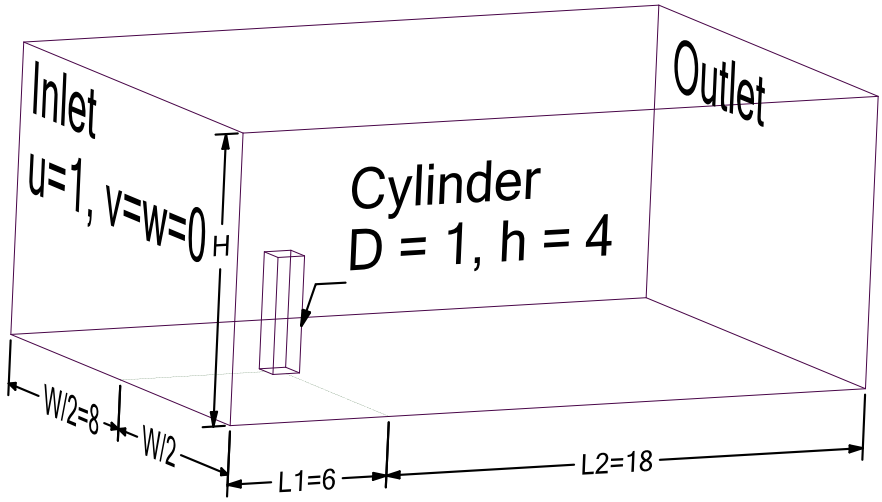

Figure A1. Computational domain of the validation case.

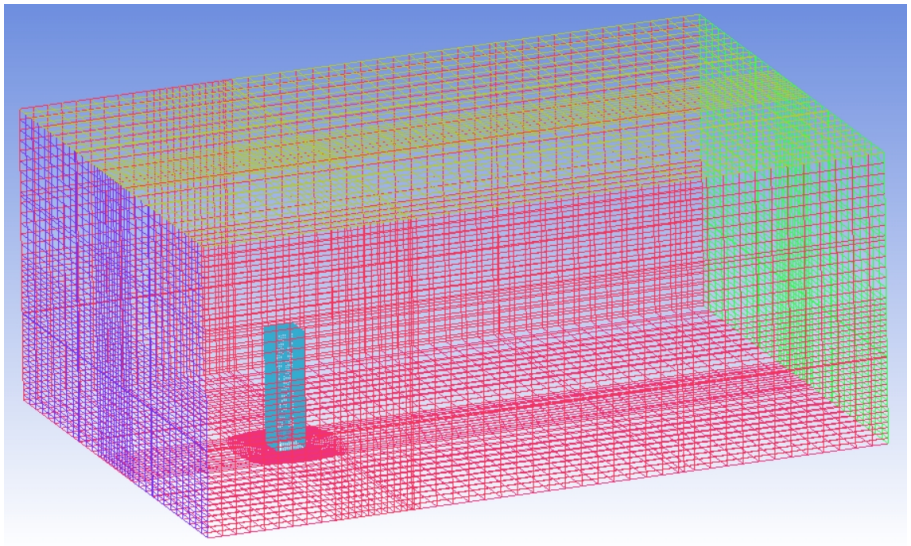

Figure A2. Computational mesh M4 for validation case. O-block was applied to refine the mesh around the cylinder.

Table A1. Mesh independence study and validation for a square cylinder of $AR = 4$.

Name	Grid Resolution	Element Number $\times 10^5$	$N_x \times N_y \times N_z$	Time Step	Mean Drag Coefficient, Re = 250
M1	192 × 136 × 124 [a]	1.81 [b]	32 × 32 × 64 [c]	0.00625	1.264
M2	200 × 144 × 140	2.44	40 × 40 × 80	0.00500	1.243
M3	208 × 152 × 156	3.24	48 × 48 × 96	0.00417	1.234
M4	216 × 160 × 172	4.23	56 × 56 × 112	0.00300	1.230
Ming's Level-1	215 × 148 × 125	39.8	32 × 32 × 77	0.002	1.186
Ming's Level-2	244 × 171 × 148	61.8	39 × 39 × 93	0.001	1.208
Ming's Level-3	262 × 185 × 170	82.4	42 × 42 × 104	0.0008	1.213
Saha's Coarse Level	152 × 112 × 98	16.6	26 × 26 × 71	0.002	1.19
Saha's Middle Level	177 × 136 × 120	28.9	34 × 34 × 83	0.002	1.23
Saha's Refined Level	204 × 150 × 132	40.4	42 × 42 × 92	0.002	1.23

[a,b,c] For the present results obtained by NEK5000 using meshes M1–M4, the grid point number here is for the actual mesh that takes into account the GLL points, calculated as the initial hex20 element number × (polynomial order + 1), which is for the convenience of comparison with other studies based on the finite element method.

Pressure and Velocity Distribution

This section examines the variation of pressure and velocity distribution with changing AoA.

The pressure distribution provides insight into the force distribution on the dorsal fin. Here, the pressure is non-dimensionalised as $p^* = p/(\rho U^2)$. The pressure distribution is shown in Figure A3. As the dorsal fin rotates to higher AoA, the pressure distribution changes significantly. At AoA $= 0°$, positive pressure is observed on the surface facing the incoming flow. At AoA $= 15°$, positive pressure is still present on the upstream side, while negative pressure appears on the downstream side. The magnitudes of both positive and negative pressure increase as AoA rises.

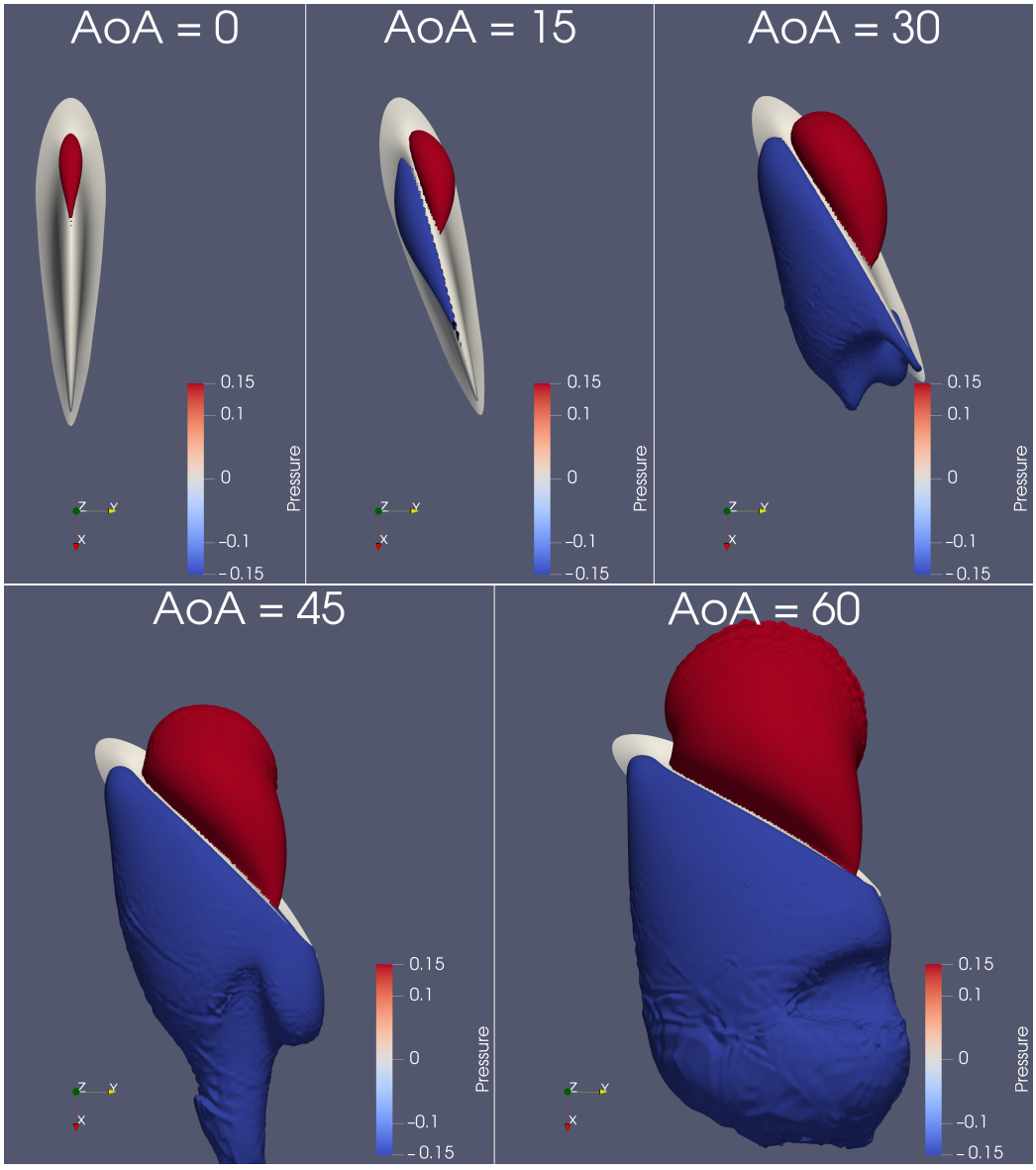

Figure A3. At $Re = 1000$ and AoA = 0–60, isosurface of $p^* = 0.15$ and -0.15 coloured by pressure magnitude, viewed from top.

Isosurfaces of local velocity magnitude $V = \sqrt{u^2 + v^2 + w^2}$ are useful for analysing the velocity aspects of the flow structure and serve as an indicator of local kinetic energy. Two isosurfaces of velocity magnitudes $V = 0.5$ and $V = 1.0$ are plotted in Figure A4. As the AoA increases, the isosurface of $V = 0.5$ shows little variation, while the isosurface of $V = 1.0$ forms a noticeable bump on the upstream side. This bump grows significantly as the AoA increases from 0° to 60°.

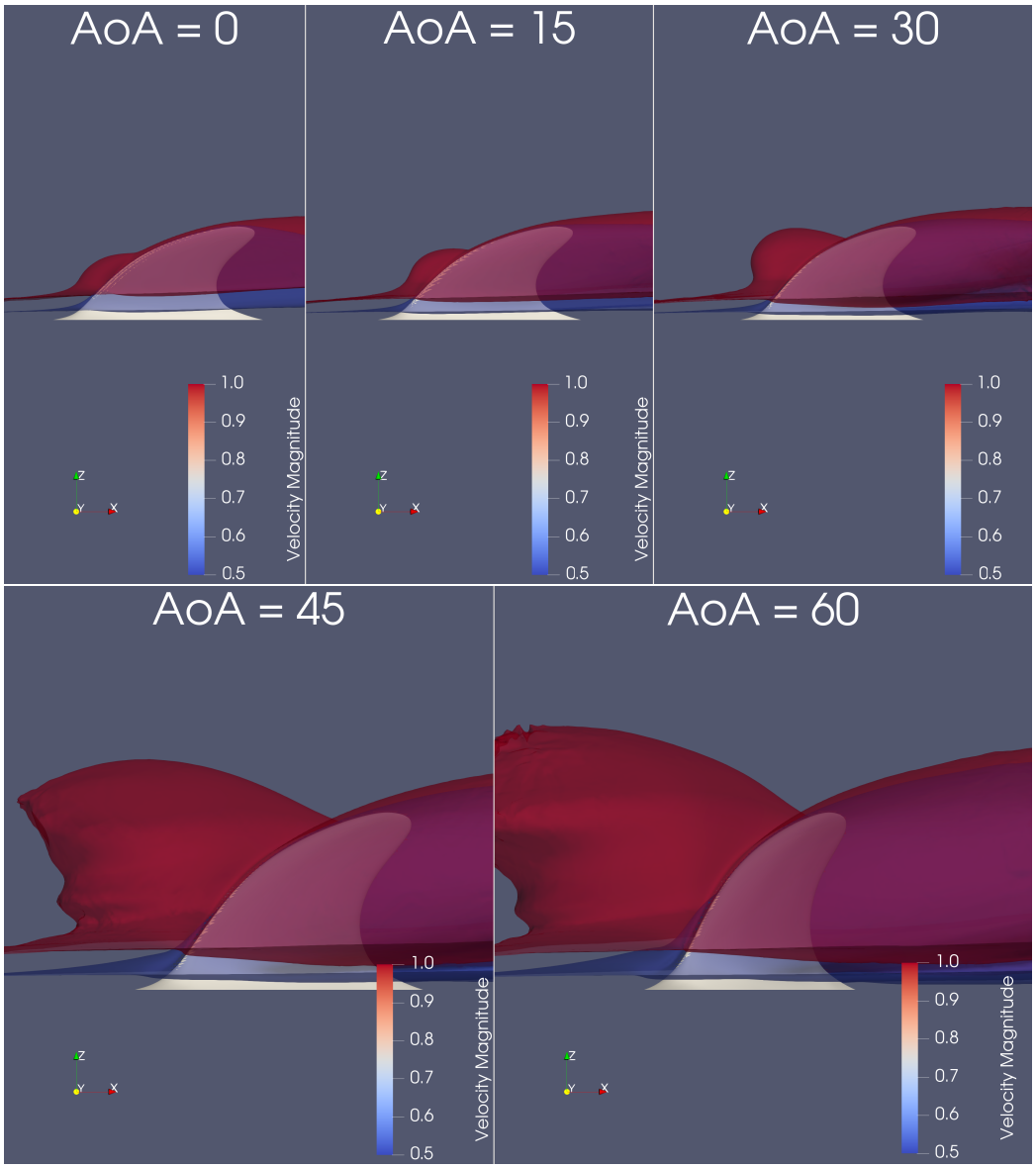

Figure A4. At $Re = 1000$ and AoA = 0–60°, isosurface of $p^* = 0.15$ and -0.15 coloured by velocity magnitude, viewed from the side.

Appendix B. Additional Data

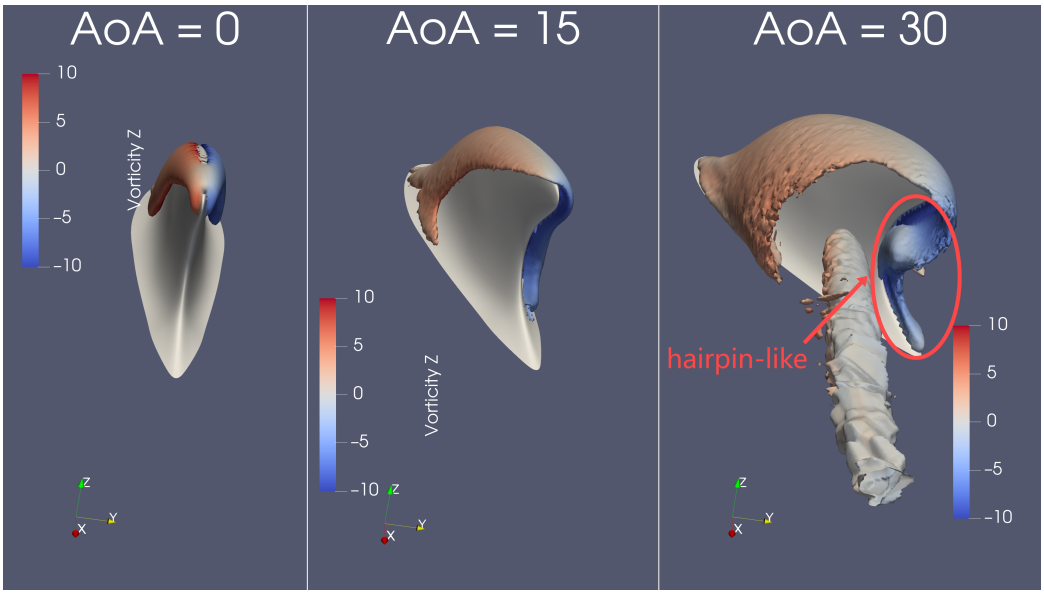

Figure A5. At $Re = 1000$ and AoA = 0–60°, the isosurface of $Q^* = 7.7$ coloured by z-vorticity, viewed from the back. A hairpin-like vortex can be observed at both AoA = 30° and 45°. Also, a clear wake vortex can be found in the downstream region.

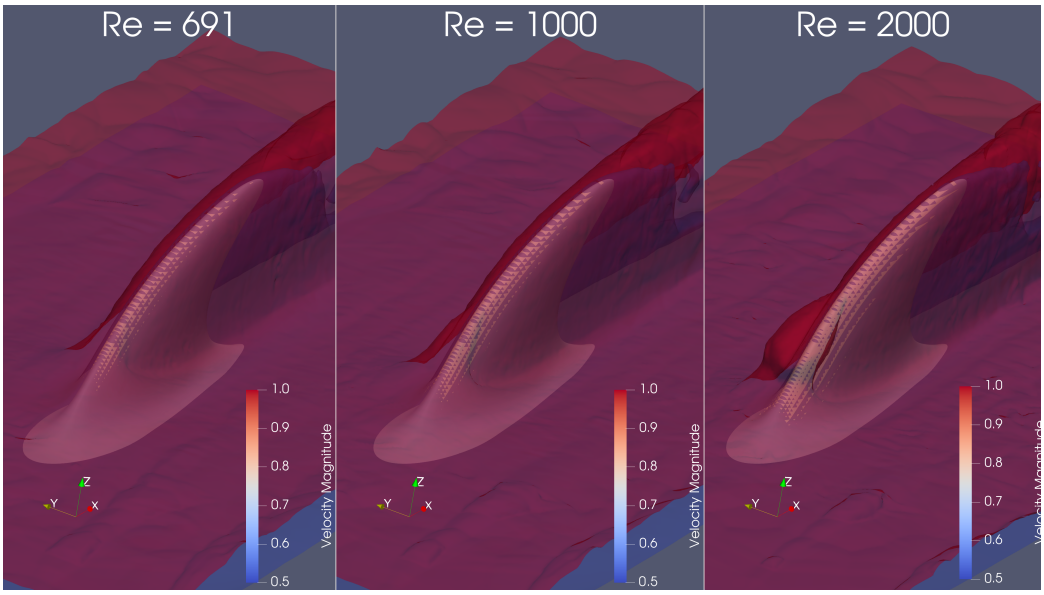

Figure A6. At AoA = 0° and Re = 691–2000, the perspective view for isosurfaces of velocity magnitude is shown. The red and blue surfaces stand for where local velocity magnitude V equals 1 and 0.5 times the inlet velocity magnitude U.

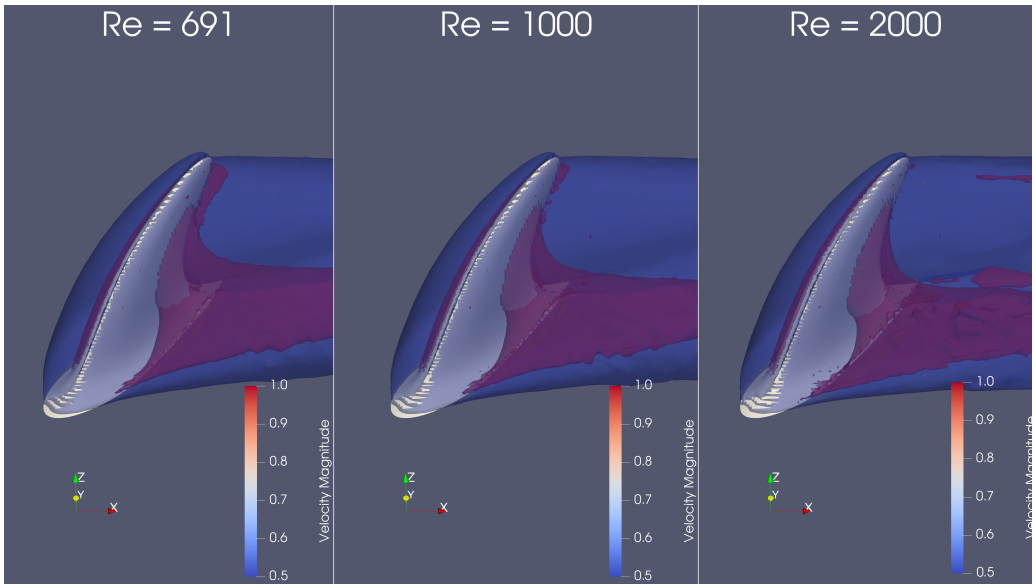

Figure A7. At AoA = 60° and *Re* = 691–2000, perspective view for isosurfaces of velocity magnitude is shown.

References

1. Shoele, K.; Zhu, Q. Drafting mechanisms between a dolphin mother and calf. *J. Theor. Biol.* **2015**, *382*, 363–377. [CrossRef] [PubMed]
2. Weihs, D. The Hydrodynamics of Dolphin Drafting. *J. Biol.* **2004**, *3*, 8. [CrossRef] [PubMed]
3. Yu, J.; Wang, T.; Chen, D.; Meng, Y. Quantifying the Leaping Motion Using a Self-Propelled Bionic Robotic Dolphin Platform. *Biomimetics* **2023**, *8*, 21. [CrossRef] [PubMed]
4. Fish, F.E.; Rohr, J. *Review of Dolphin Hydrodynamics and Review of Dolphin Hydrodynamics* ; Technical Report; Space and Naval Warfare Systems Command: San Diego, CA, USA, 1999. Available online: https://apps.dtic.mil/sti/citations/ADA369158 (accessed on 7 September 2024).
5. Wang, J.; Pavlov, V.; Lou, Z.; Dong, H. Computational investigation of thrust production of a dolphin at various swimming speeds. In Proceedings of the American Society of Mechanical Engineers, Fluids Engineering Division (Publication) FEDSM, Virtual, Online, 10–12 August 2021; Volume 1. [CrossRef]
6. Wang, J.; Wu, Z.; Tan, M.; Yu, J. Controlling the depth of a gliding robotic dolphin using dual motion control modes. *Sci. China Inf. Sci.* **2020**, *63*, 192206. [CrossRef]
7. Han, P.; Wang, J.; Fish, F.E.; Dong, H. Kinematics and Hydrodynamics of a Dolphin in Forward Swimming. In Proceedings of the AIAA AVIATION 2020 FORUM (2020), Virtual Event, 15–19 June 2020; p. 3015. [CrossRef]
8. Pavlov, V.; Vincent, C.; Mikkelsen, B.; Lebeau, J.; Ridoux, V.; Siebert, U. Form, function, and divergence of a generic fin shape in small cetaceans. *PLoS ONE* **2021**, *16*, e0255464. [CrossRef]
9. Fish, F.E.; Howle, L.E.; Murray, M.M. Hydrodynamic flow control in marine mammals. *Integr. Comp. Biol.* **2008**, *48*, 788–800. [CrossRef]
10. Niño-Torres, C.A.; Olvera-Gómez, J.A.; Ramos, E.; Castelblanco-Martínez, D.N.; Blanco-Parra, M.P.; May-Collado, L.J.; Sellares, R. High similarities in dorsal fin ratios of common bottlenose dolphins (Tursiops truncatus) in the Caribbean Sea. *Mar. Mammal Sci.* **2023**, *39*, 533–552. [CrossRef]
11. Li, S.; Wu, Z.; Wang, J.; Qiu, C.; Tan, M.; Yu, J. Robust Depth and Heading Control System for a Novel Robotic Dolphin With Multiple Control Surfaces. *IEEE Trans. Autom. Sci. Eng.* **2024**, 1–16. [CrossRef]
12. Bashtani, I.; Esfahani, J.A.; Kim, K.C. Hybrid CFD-ANN approach for evaluation of bio-inspired dolphins dorsal fin turbulators of heat exchanger in turbulent flow. *Appl. Therm. Eng.* **2023**, *219*, 119422. [CrossRef]
13. Rahmani, M.; Jafari Gavzan, I.; Dehghan Manshadi, M. Experimental investigation of the effect of sail geometry on the flow around the SUBOFF submarine model inspired by the dolphin's dorsal fin. *Ships Offshore Struct.* **2024**, *19*, 769–778. [CrossRef]
14. Guo, J.; Zhang, W.; Han, P.; Fish, F.E.; Dong, H. Thrust generation and propulsive efficiency in dolphin-like swimming propulsion. *Bioinspir. Biomim.* **2023**, *18*, 056001. [CrossRef] [PubMed]
15. Bergmann, M. Numerical modeling of a self-propelled dolphin jump out of water. *Bioinspir. Biomim.* **2022**, *17*, 065010. [CrossRef] [PubMed]
16. Skrovan, R.C.; Williams, T.M.; Berry, P.S.; Moore, P.W.; Davis, R.W. The diving physiology of bottlenose dolphins (Tursiops truncatus): II. Biomechanics and changes in buoyancy at depth. *J. Exp. Biol.* **1999**, *202*, 2749–2761. [CrossRef]
17. Wu, Z.; Yu, J.; Yuan, J.; Tan, M. Towards a gliding robotic dolphin: Design, modeling, and experiments. *IEEE/ASME Trans. Mechatron.* **2019**, *24*, 260–270. [CrossRef]

18. Zhang, Y.; Wu, Z.; Wang, J.; Tan, M. Design and Analysis of a Bionic Gliding Robotic Dolphin. *Biomimetics* **2023**, *8*, 151. [CrossRef]
19. Pavlov, V.V.; Rashad, A.M. A non-invasive dolphin telemetry tag: Computer design and numerical flow simulation. *Mar. Mammal Sci.* **2012**, *28*, E16–E27. [CrossRef]
20. Okamura, T.; Akune, Y.; Mori, T.; Morisaka, T.; Otomo, W.; Wakabayashi, I.; Watanabe, S.; Yoda, K. Contribution of flippers and dorsal fins to the lateral/directional inherent stability during straight-line swimming in small cetaceans. *J. Zool.* **2021**, *315*, 165–174. [CrossRef]
21. Tanaka, H.; Li, G.; Uchida, Y.; Nakamura, M.; Ikeda, T.; Liu, H. Measurement of time-varying kinematics of a dolphin in burst accelerating swimming. *PLoS ONE* **2019**, *14*, e0210860. [CrossRef]
22. Noren, S.R.; Biedenbach, G.; Redfern, J.V.; Edwards, E.F. Hitching a ride: The formation locomotion strategy of dolphin calves. *Funct. Ecol.* **2008**, *22*, 278–283. [CrossRef]
23. Tawade, J.V.; Biradar, M.M.; Benal, S.S. A new approach of MHD flows for UCM fluid over a permeable moving plate with space and temperature dependent internal heat generation/absorption. *AIP Conf. Proc.* **2020**, *2236*, 060002 . [CrossRef]
24. Zhong, Q.; Dong, H.; Quinn, D.B. How dorsal fin sharpness affects swimming speed and economy. *J. Fluid Mech.* **2019**, *878*, 370–385. [CrossRef]
25. Fischer, P.; Lottes, J.; Tufo, H. *Nek5000*; Technical Report; Argonne National Laboratory (ANL): Argonne, IL, USA, 2007.
26. Quartapelle, L. *Numerical Solution of the Incompressible Navier-Stokes Equations*; Birkhäuser: Basel, Switzerland, 2012; International Series of Numerical Mathematics, Volume 113.
27. Abouhussein, A.; Peet, Y.T. Computational framework for efficient high-fidelity optimization of bio-inspired propulsion and its application to accelerating swimmers. *J. Comput. Phys.* **2023**, *482*, 112038. [CrossRef]
28. Patera, A.T. A spectral element method for fluid dynamics: Laminar flow in a channel expansion. *J. Comput. Phys.* **1984**, *54*, 468–488. [CrossRef]
29. Karniadakis, G.; Sherwin, S. *Spectral/hp Element Methods for Computational Fluid Dynamics*; Oxford University Press: Cary, NC, USA, 2007. [CrossRef]
30. Fischer, P.F. *Implementation Considerations for the OIFS/Characteristics Approach to Convection Problems*; Argonne National Laboratory: Argonne, IL, USA, 2003.
31. Rezaeiravesh, S.; Jansson, N.; Peplinski, A.; Vincent, J.; Schlatter, P. Nek5000 Theory, Implementation and Optimization. KTH, FLOW-SESE Course, 2021. Available online: https://www.mech.kth.se/~pschlatt/Nek5000_2021.pdf (accessed on 7 September 2024).
32. Tufo, H.M.; Fischer, P.F. Fast Parallel Direct Solvers for Coarse Grid Problems. *J. Parallel Distrib. Comput.* **2001**, *61*, 151–177. [CrossRef]
33. Saha, A.K. Unsteady flow past a finite square cylinder mounted on a wall at low Reynolds number. *Comput. Fluids* **2013**, *88*, 599–615. [CrossRef]
34. Zhang, D.; Cheng, L.; An, H.; Zhao, M. Direct numerical simulation of flow around a surface-mounted finite square cylinder at low Reynolds numbers. *Phys. Fluids* **2017**, *29*, 045101. [CrossRef]
35. Rastan, M.R.; Sohankar, A.; Alam, M.M. Low-Reynolds-number flow around a wall-mounted square cylinder: Flow structures and onset of vortex shedding. *Phys. Fluids* **2017**, *29*, 103601. [CrossRef]
36. Martínez-Sánchez, Á.; López, E.; Le Clainche, S.; Lozano-Durán, A.; Srivastava, A.; Vinuesa, R. Causality analysis of large-scale structures in the flow around a wall-mounted square cylinder. *J. Fluid Mech.* **2023**, *967* . [CrossRef]

Disclaimer/Publisher's Note: The statements, opinions and data contained in all publications are solely those of the individual author(s) and contributor(s) and not of MDPI and/or the editor(s). MDPI and/or the editor(s) disclaim responsibility for any injury to people or property resulting from any ideas, methods, instructions or products referred to in the content.